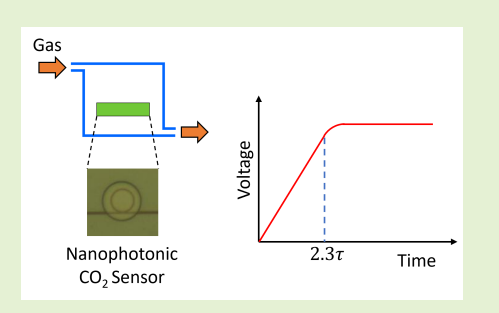


Dynamic Characterization of a Fast-responding Nanophotonic Gas Sensor using Optimization-based System Identification

Bibek Ramdam*, Eman M. Abdelazim*, Hyun-Tae Kim, Hosam K. Fathy, and Miao Yu

Abstract—This paper develops and parameterizes a dynamic model of a novel nanophotonic gas sensor. The sensor employs a functionalized microring resonator to measure CO₂ concentrations in biomedical applications. The literature presents both computational and experimental approaches for characterizing nanophotonic sensor response times. However, it can be challenging to distinguish between the dynamics of a fast-responding sensor versus the dynamics of the setup used for characterizing it. We address this challenge using optimization-based system identification. Specifically, we construct a test rig that supplies mixed N₂/CO₂ flow to the sensor and measures the sensor's voltage amplitude response at a given laser excitation wavelength. Step response experiments are conducted using this test rig, at different gas flowrates and concentrations. A state-space model is



then constructed, capturing the sensor's first-order dynamics as well as the gas transport, manifold filling, and first-order valve actuator dynamics of the test setup. A particle swarm optimizer is used for least-squares model parameterization. The resulting residuals are reasonable in magnitude, two observations being that their magnitude changes with CO_2 concentration and that they exhibit some coloring, potentially due to the setup's signal processing filters. The estimated time constant has reasonable Cramér-Rao bounds, and is close in magnitude to finite element predictions.

Index Terms— Gas sensors; nanophotonics; sensor dynamics; system identification.

I. Introduction

Nanotechnology has played a vital role in advancing optical gas sensors [1]–[3]. In recent years, metal organic frameworks (MOFs), which possess a nanoporous structure capable of selectively adsorbing specific gas molecules [4], [5], have received significant attention for their ability to enhance the sensing performance of both refractive index (RI)-based [6]–[10] and infrared absorption-based gas sensors [10]-[14]. When a MOF layer is applied to the optical path of a gas sensor, the interaction between light and the target gas is greatly enhanced due to the selective adsorption of the gas molecules on the expansive surface area of the nanoporous MOF. This enhanced light-gas interaction improves the sensitivity and lowers the detection limit of the sensor. Furthermore, a thin-film MOF coating layer, typically measuring just a few micrometers in thickness, results in a short gas diffusion time, enabling the development of fast-responding optical gas sensors. However, precise characterization of such fast-responding gas sensors

*Equal contributions.

Submitted on November 22, 2023. This work was funded by the U.S. National Science Foundation's Growing Convergence Research program, through NSF GCR Award #2121110. The authors gratefully acknowledge this support.

All authors are with the Mechanical Engineering Department at The University of Maryland, College Park. Bibek Ramdam and Eman M. Abdelazim are Ph.D. students. Hyun-Tae Kim is an Assistant Research Professor. Hosam K. Fathy and Miao Yu (corresponding author, mmyu@umd.edu) are Professors at UMCP.

remains a challenge. For example, recent studies on MOF-based optical gas sensors have reported a wide range of sensor response time, ranging from hundreds of milliseconds to tens of seconds [6]–[14], despite employing similar sensing mechanisms and MOF films of similar thickness and diffusivity. This discrepancy arises due to the difficulty in achieving a rapid change in gas concentration within the gas cell. Additionally, the measured time response often includes the dynamics of the gas handling system, including valve actuation for gas flow control and gas mixing/filling in the manifold and gas cell. The response of a gas handling system cannot be neglected when characterizing fast-responding gas sensors, especially those with sub-second response times.

Optimization-based system identification provides tools for estimating the parameters of coupled dynamic systems from experimental input-output data [15], [16]. Such tools have the potential to enable the simultaneous estimation of the parameters of a novel sensor plus the setup used for testing/characterizing it. This can be particularly valuable in research efforts where one seeks to characterize the dynamic response of a fast sensor in the presence of slower test setup dynamics. One goal of this work is to demonstrate such application of system identification to a novel dissolved carbon dioxide (CO₂) sensor. Specifically, we employ optimization-based system identification to characterize the response time of a novel fast-responding MOF-based optical gas sensor by analyzing the combined sensor and gas handing system. As

a proof of concept, a RI-based optical CO₂ gas sensor is developed using a silicon microring resonator coated with ZIF-8 and PDMS. Further, a state-space model that incorporates (i) the sensor, (ii) valve actuation, and (iii) gas mixing/filling dynamics is constructed. The time constant of the first-order sensor dynamics is estimated, and Cramér-Rao error bounds for this constant are determined through Fisher information analysis. It should be noted that the sensor response time, commonly defined as the time taken to reach 90% of a steadystate or maximum level (τ_{90}) , is approximately 2.3 times of the time constant (τ) [17]. To validate the accuracy of the estimated sensor response time, the dynamic gas diffusion in the sensor is simulated using a finite element method. The novelty of this paper stems from its optimization-based experimental characterization of the sub-second response time of a MOF-based optical gas sensor from combined sensor/test setup data. Furthermore, the proposed optimizationbased system identification approach enables the cost-effective characterization of various fast-responding sensors, as it allows the use of conventional test systems with significantly slower dynamic responses compared to the sensor response.

The remaining sections of this paper are organized as follows. Section II describes the design and fabrication of the dissolved CO₂ gas sensor with ZIF-8/PDMS coating, experimental setup for characterizing the sensor response time, and the results of the characterization experiments. Section III presents estimation of the time constants using the optimization-based system identification method and FEM simulations of gas diffusion. Further, it provides a discussion of the obtained results. Finally, Section IV concludes the paper.

II. SENSOR AND EXPERIMENTS

A. Sensor Design

The dissolved CO₂ gas sensor consists of a silicon ring resonator and a ZIF-8/PDMS top cladding layer, as shown in Figs. 1(a) and 1(b). The high-Q ring resonator facilitates low detection limit RI sensing [18], [19]. Moreover, the ZIF-8 cladding layer enables selective and sensitive detection of the RI change induced by CO₂ adsorption in the ZIF-8. The gaspermeable and hydrophobic PDMS coating layer allows CO₂ molecules to diffuse into and out of the ZIF-8 while separating the ZIF-8 from the sensing solution. Note that the sensing surface area is mainly determined by the ring waveguide length and the thickness of the ZIF-8 coating. As long as the ring waveguide is fully coated with a ZIF-8 film, the sensitivity is independent of the shape of the ZIF-8 coating. Further details of the sensor design and its operation principle can be found in [20]. The sensor fabrication process can be found in Sec. 1 of the Supplementary Material.

B. Experimental Test Setup

Fig. 2 shows the schematic diagram of the experimental setup for characterizing the sensor time constant. Light from a tunable laser (TSL-510, Santec) was passed through a polarization controller and coupled into the sensor using a single-mode optical fiber (SMF). The light from the sensor was collected by a fiber-optic photoreceiver (Model 2053,

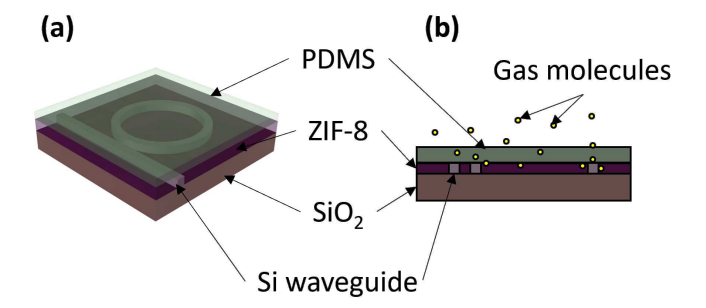


Fig. 1. Schematic showing (a) the developed dissolved ${\rm CO_2}$ sensor and (b) its cross-sectional view.

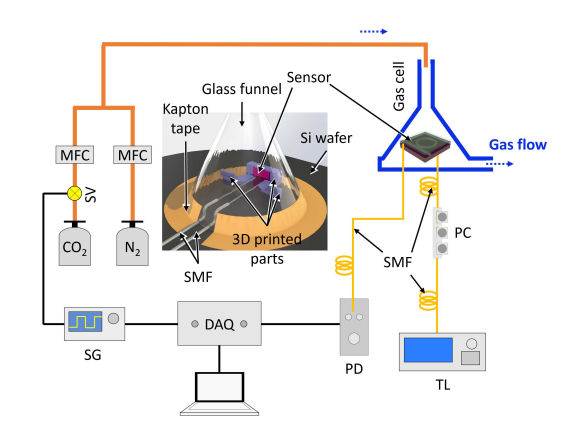


Fig. 2. Experimental setup for characterizing the time constant of the gas sensor. The inset within the figure shows the CAD rendering of the gas cell on top of the sensor. DAQ: data acquisition instrument, MFC: mass flow controllers, PC: polarization controller, PD: photodetector, SG: signal generator, SMF: single mode fiber, SV: solenoid valve, TL: tunable laser.

New Focus) and the output voltage of the photoreceiver was logged using a data acquisition system (Picoscope 6000, Pico Technology) with a sampling rate of 1 millisecond.

 N_2 and CO_2 were used as the carrier and test gases, respectively. The flow rates of both gases were regulated using mass flow controllers (MFCs) (N_2 : 6A0107BV-NC, CO_2 : 6A0107SV-CA, Dakota Instruments). Moreover, a solenoid valve (2W-025-08, ATO Inc), operated using a function generator (AFG3102C, Tektronix) was integrated between the CO_2 gas cylinder and its MFC to control the timing of CO_2 gas flow. The CO_2 and N_2 gas flows from the MFCs were combined using a connector tube and were fed into the gas cell, as shown in the inset within Fig. 2. The entire experiment was performed under room temperature and atmospheric pressure conditions. Additionally, before the experiment the sensor was placed in N_2 flow for 12 hours to stabilize its signal.

C. Characterization Experiments

An experimental dataset with varying CO_2 concentrations and total gas flowrates is required for the optimization-based system identification. Note that N_2 flowrate does not need to be constant if varying total flowrates are achieved. Table I shows the seven experimental conditions that were used for sensor characterization. The experiment examined three CO_2 concentrations of 11.1%, 14.3%, and 16.7%. For 11.1% and

14.3% CO₂ concentrations, two different gas flow rates were examined whereas three different flow rates were tested for 16.7% CO₂ concentration.

Figs. 3(a), 3(c), and 3(e) show the transmission spectra of the sensor at CO₂ concentrations of 11.1%, 14.3%, and 16.7%, respectively. In each figure, the solid black curve represents the sensor's response to 0% CO₂ concentration (i.e., pure N₂ flow). The red colored curves represent the sensor's response to one of the total flow rates, which is the sum of CO2 and N2 flow rates. The green arrow indicates the excitation wavelength of 1574.400 nm used for characterizing the dynamic response of the sensor. The excitation wavelength of 1574.4 nm, which is located close to the largest slope of the resonance, was chosen because it provides a large intensity modulation in response to the resonance shift induced by CO₂ concentration changes. The transmission spectra exhibit that the resonance wavelength redshifts with increasing CO₂ concentration. These redshifts result from the increase in the refractive index of the ZIF-8 cladding induced by CO₂ adsorption. Note that the three CO₂ concentration levels and the excitation wavelength of 1574.400 nm were selected based on the conditions as follows. Firstly, the sensor is operated within the linear region of the resonance curve. Additionally, to accommodate the manual operation of the MFCs, which have the smallest division of 1 L/min in their measurement scales, the flow rate is controlled with approximately 0.5 L/min increment for reasonable accuracies.

The voltage responses of the sensor to changes in CO₂ concentration are shown in Figs. 3(b), 3(d), and 3(f). In each figure, the solid black line represents the driving signal from the function generator that controls the solenoid valve operation. Initially, the valve was in a closed state at 0 V, i.e., CO₂ gas was not flowing into the gas cell. It switched to an open state, allowing CO₂ gas to flow in the gas cell, when the signal changed to 3.3 V. The other colored curves represent the sensor's response at different total flow rates, synchronized with the driving signal.

The response curves show that there is a delay between the driving signal and the sensor response. This delay decreased as the total flow rate increased. Moreover, the sensor response reached its maximum voltage faster with an increasing flow rate. This flowrate dependency is believed to result from the gas transport delay and the manifold mixing of CO2 and O2 gases. Additionally, the sensor response includes a flow rate independent delay resulting from the physical opening/closing process in the solenoid valve actuation. Note that the voltage change induced by the resonance wavelength shift should be the same for the same CO₂ concentration experiment regardless of the total flow rates. However, the experimental results, as shown in Figs. 3(b), 3(d) and 3(f), reveal that the resonance shifts were not consistent across different total flow rates. This inconsistency arises because the actual CO₂ concentrations at different total flow rates deviate from the nominal value. This discrepancy is attributed to the difficulty in precisely controlling CO₂ and O₂ flow rate with an increment 0.5 L/min increment using the manual MFCs. To address this problem, electronic MFCs with a high precision can be employed to achieve better control and eliminate this error.

III. MODELING AND PARAMETERIZATION

A. State-Space Model

The remainder of this paper assumes that the coupled dynamics of the sensor plus its test setup are governed by the third-order, lumped-parameter state-space model derived below. We begin by deriving the governing equations for this model based on physical first principles, then utilize it for sensor characterization.

Fig. 4 provides a conceptual representation of the dynamics captured by the proposed model. We assume the experimental setup supplies N_2 and CO_2 at two volumetric flowrates, Q_{N_2} and Q_{CO_2} , respectively. Mixing these two flows furnishes a volumetric CO_2 concentration equal to $c_{CO_2} = Q_{CO_2}/Q$, where the total volumetric flowrate, Q, is given by:

$$Q = Q_{N_2} + Q_{CO_2} \tag{1}$$

We assume that over the course of a given sensor characterization experiment, the above CO_2 concentration changes between some user-prescribed maximum and minimum values, c_{max} and c_{min} , respectively. It is convenient to define a dimensionless indicator function, $x_1(t)$, that goes from 0 to 1 as this concentration goes from its minimum to its maximum value, respectively. Mathematically, one can relate CO_2 concentration to this indicator function as follows:

$$c_{CO_2} = c_{min} + (c_{max} - c_{min})x_1 \tag{2}$$

Now we assume that the user-specified, desired CO_2 concentration is some function, $c_{CO_2}^{des}(t)$, where t denotes time. This desired CO_2 concetration is achieved through the control of a valve actuation system, as shown in the setup's schematic. It is important to note that this valve actuation's response to the control signal will not be instantaneous, since the valves will have their own dynamics. Assuming, for simplicity, that these dynamics are governed by linear first-order behavior leads to the followig state equation:

$$\frac{dc_{CO_2}}{dt} = \frac{1}{\tau_v} (c_{CO_2}^{des} - c_{CO_2}),\tag{3}$$

where τ_v is the actuation time constant. Substituting Eq. 2 into Eq. 3 gives:

$$\dot{x}_1 = \frac{1}{\tau_v} \frac{c_{CO_2}^{des} - c_{CO_2}}{c_{max} - c_{min}} \tag{4}$$

The above equation can now be rewritten as follows:

$$\dot{x}_1 = \frac{1}{\tau_v} (u - x_1),\tag{5}$$

where u(t) is itself a dimensionless indicator function that goes from 0 to 1 as the user-commanded CO_2 concentration goes from c_{min} to c_{max} , and is related to $c_{CO_2}^{des}$ as follows:

$$c_{CO_2}^{des} = c_{min} + (c_{max} - c_{min})u(t)$$
 (6)

TABLE I SUMMARY OF EXPERIMENTAL CONDITIONS

Experiment #	1	2	3	4	5	6	7
Total Flowrate (L/min)	4.5	3.5	3.0	9.0	7.0	6.0	9.0
N ₂ Flowrate (L/min)	4.0	3.0	2.5	8.0	6.0	5.0	7.5
CO ₂ Flowrate (L/min)	0.5	0.5	0.5	1.0	1.0	1.0	1.5
CO ₂ conc. %	11.1	14.3	16.7	11.1	14.3	16.7	16.7

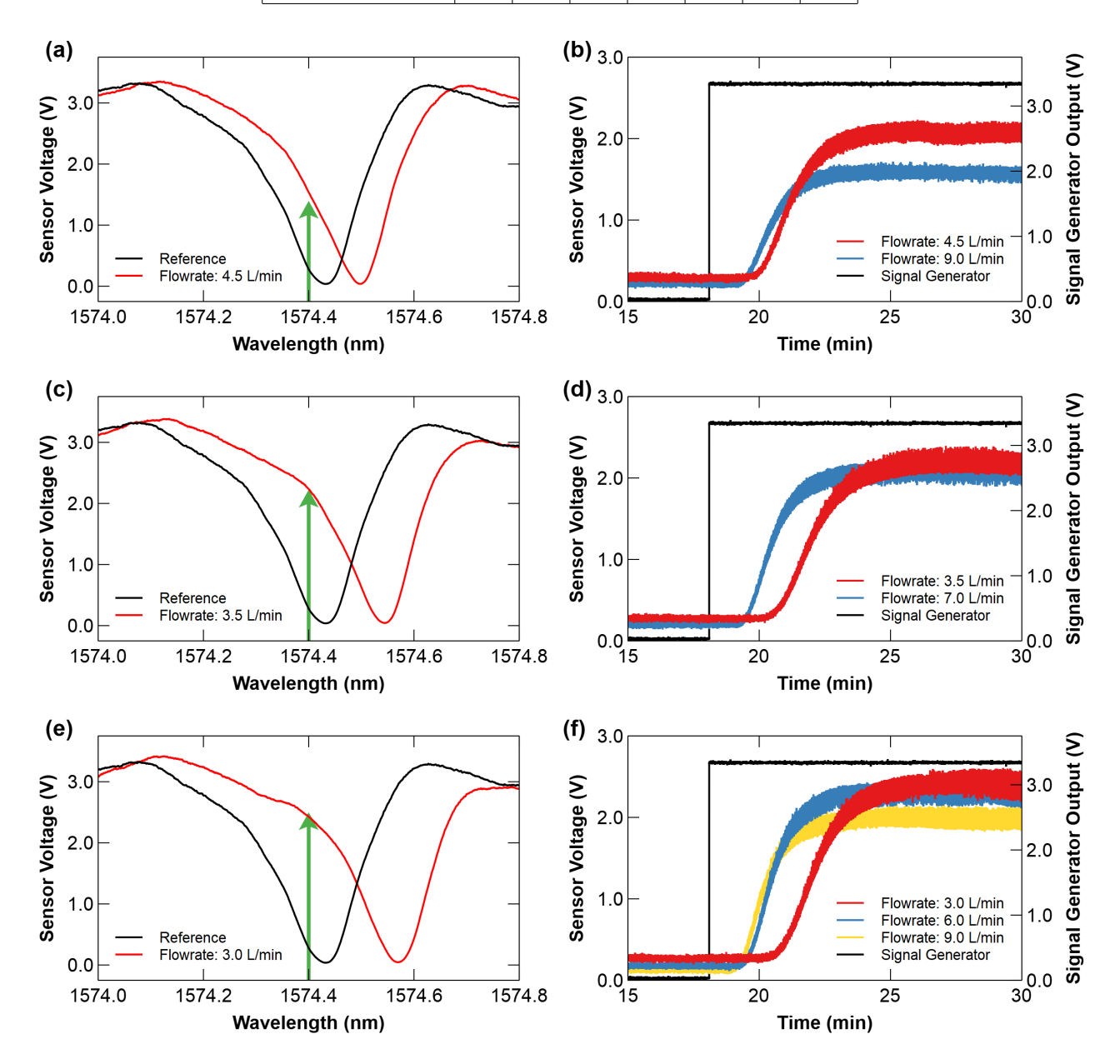


Fig. 3. Transmission spectra of the sensor measured at (a) 11.1%, (c)14.3%, and (e) 16.7% CO_2 concentrations. The green arrow represents the excitation wavelength of 1574.400 nm. Dynamic responses of the sensor at different flowrates for changes in CO_2 concentration from 0% to (b) 11.1%, (d)14.3%, and (f) 16.7%. Due to the limitations of the MFC's, it was not possible to keep a constant total flow rate in our experiments. However, it should be noted that the resonance shifts were induced by changes in CO_2 concentration and remain unaffected by gas flow rate.

The dimensionless, normalized input command u(t) depends on the particular sensor characterization experiment at hand. In an experiment where the user requests a step change from minimum to maximum CO_2 concentration at some time

 t_o , followed by a return to minimum concentration at some time t_f , one can express u(t) as follows:

$$u(t) = \mathcal{U}(t - t_0) - \mathcal{U}(t - t_f) \tag{7}$$

where $\mathcal{U}()$ is the unit step function.

Now we assume that the fluid mixture generated by the valve system enters a manifold of volume V. Moreover, we assume that flow through this manifold is incompressible. Finally, we assume that the dimensionless, normalized concentration of CO_2 in this manifold is given by some indicator function, $x_2(t)$. Then the law of conservation of mass states that the rate of change of the mass of CO_2 in this manifold must equal the rate at which CO_2 enters the manifold minus the rate at which it is ejected from the manifold. Expressing this law in terms of nomrmalized, dimensionless concentration variables leads to the following equation:

$$V\dot{x}_2 = Qx_1 - Qx_2$$

$$\implies \dot{x}_2 = \frac{Q}{V}(x_1 - x_2)$$
(8)

Now we assume that this paper's sensor is exposed to the output of the above manifold mixing process. Moreover, we assume that the sensor can be represented as a simple lumped volume, V_s , where the dimensionless concentration of CO_2 inside this volume is $x_3(t)$. Finally, we assume that the transport of gas between this lumped vollume and its surroundings is governed by Fick's law of diffusion. Then the dynamics of the normalized CO_2 concentration inside the sensor volume are governed by the law of conservation of mass, as follows:

$$V_s \dot{x}_3 = \frac{D_s A_s}{T_s} (x_2 - x_3), \tag{9}$$

where D_s is the effective lumped sensor diffusivity, A_s is the effective sensor diffusion area, and T_s is the effective sensor diffusion thickness. Grouping terms allows the above equation to be rewritten as follows:

$$\dot{x}_3 = \frac{1}{\tau}(x_2 - x_3),\tag{10}$$

where $\tau = T_s V_s/D_s A_s$ is the sensor's time constant. The goal of this work is to estimate this time constant from sensor characterization experiments. The input to these characterization experiments, u(t), is a user-commanded change in normalized CO_2 concentration. The output is the voltage signal produced by the sensor. For a sufficiently small range of CO_2 concentrations, we approximate this voltage as an affine (i.e., constant plus linear) function of the normalized CO_2 concentration, $x_3(t)$, seen by the sensor:

$$y = y_0 + \beta x_3 \tag{11}$$

Altogether, the above equations constitute a state-space model that can be used for sensor characterization. The model contains three state equations plus one output equation, as summarized below:

$$\dot{x}_1 = \frac{1}{\tau_v} (u - x_1), \quad \dot{x}_2 = \frac{Q}{V} (x_1 - x_2)
\dot{x}_3 = \frac{1}{\tau} (x_2 - x_3), \quad u(t) = \mathcal{U}(t - t_o) - \mathcal{U}(t - t_f)
y = y_o + \beta x_3$$
(12)

Sensor characterization can now be formulated as an exercise in estimating the above model's parameters, as discussed below.

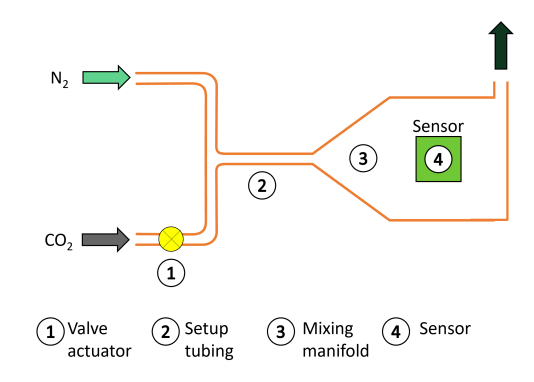


Fig. 4. Schematic representation of sensor model.

B. System Identification

Seven experimental data sets were used for estimating the parameters of the above state-space model. In all of these experiments, CO₂ concentration was switched between zero and a nonzero maximum value. Table I shows the total volumetric gas flowrate plus the maximum CO₂ concentration for each experiment. System identification was performed over all 7 experiments simultaneously. Specifically, we used the Matlab implementation of the particle swarm optimization algorithm to minimize the quadratic sensor voltage prediction error, summed over all sampling time instants in all 7 experiments, subject to the above state-space sensor model. The model was simulated with a 1-millisecond time step, equal to the experimental sampling time, using the first-order forward Euler integration method, assuming zero initial conditions for all state variables. The list of optimization variables included: τ_v , V, τ , in addition to experiment-dependent values of t_o , t_f , y_o , and β . Including the instants in time, t_o and t_f , in the optimization is important because it allows the optimizer to account for potential pure time delays between the moments in time the user commands a step change in CO₂ concentration versus the moment in time the actuator initiates this step change. Potential discrepancies between these two sets of time instants can be caused by a number of factors, including actuator stick/slip behavior. Moreover, allowing the parameters y_o and β to be experiment-dependent makes it possible to characterize the sensor time constant even in the presence of effects such as voltage drift from one experiment to the next. The optimizer converged to an interior optimal solution for this system identification problem, meaning that none of the model parameter estimates hit a user-specified bound.

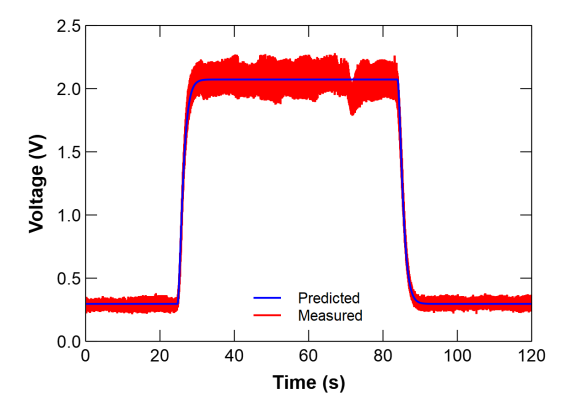


Fig. 5. Representative identified sensor model response compared with the sensor response obtained in the experiment (Experiment #1).

Fig. 5 demonstrates the quality of the curve fit obtained using the above optimization procedure, for the first of 7 sensor cycling experiments while the rest are shown in Figure S1 of the Supplementary Material. A good quality of fit is obtained across the board, for all 7 experiments. This quality of fit corresponds to a root mean square sensor voltage prediction error of 65.3 mV, across all 7 experiments. Fig. 6 provides additional details by showing the statistical distribution of the voltage prediction error, across all 7 experiments. Again, the prediction errors are reasonable, reflecting a good quality of fit.

The optimal parameter estimates obtained from the above study highlight the value of the proposed system identification approach. Three different sets of parameters were estimated by the particle swarm optimizer. First, the optimizer estimated the time constants associated with the sensor, the setup's first-order actuator dynamics, and the setup's manifold filling dynamics. The sensor's time constant, τ , was estimated to be 48.1 ms, whereas the setup's actuation time constant, τ_v , was estimated to be 857.7 ms, and the setup's manifold volume, V, was estimated to be 58.23 mL. Note that τ and τ_v are independent of the gas flow rate and that V was physically measured to be approximately 60 mL: a fact that highlights the success of this optimization effort. These parameter estimates highlight the fact that the setup's dynamics are much slower than those of the sensor. Specifically, the actuation dynamics have a time constant that is almost 18 times slower than the sensor's estimated time constant. Moreover, the flowratedependent manifold filling dynamics, even for the fastest flowrate of 9 L/min., have a slow time constant of 388ms. Together, these values show the difficulty of estimating the sensor's time constant independently, without accounting for the dynamics of the surrounding setup: a fact that underscores the value and importance of this paper's approach.

The second set of parameters estimated by the particle swarm optimizer consisted of the experiment-dependent start and end times for the experimental CO_2 step changes - namely, t_o and t_f , for each experiment, respectively. A plot of the start time and end time delays for each experiment with respect to the commanded flowrates and CO_2 concentration is shown in Fig. 7(a). Particularly Fig. 7(b) suggests that these delays

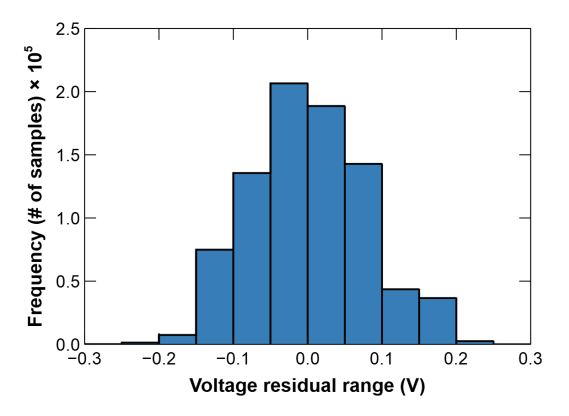


Fig. 6. Distribution of sensor voltage estimation/prediction errors (bin size: 0.05 V).

TABLE II
ESTIMATED PARAMETERS OF VOLTAGE CHARACTERISTICS

Exp. #	1	2	3	4	5	6	7
$y_o(V)$	0.296	0.267	0.263	0.219	0.194	0.175	0.121
β (V) %	1.78	1.92	2.13	1.41	1.88	2.11	1.85
t_o (s)	24.6699	20.3555	25.3647	31.0635	29.3724	30.1734	24.5127
t_f (s)	83.8527	79.3072	84.7885	89.5093	88.9165	89.9908	84.1776

could be flowrate dependent. Linear regression models are constructed as $t_{oc} - t_o = \hat{a_0} + \hat{a_1}1/Q$, and $t_{of} - t_f =$ $b_0 + b_1 1/Q$ to express the delay in start and end times $t_{oc} - t_o$ and $t_{fc} - t_f$, respectively. Both t_{oc} and t_{fc} represent the commanded start and end times in the experiments, respectively. Both linear functions have the explanatory variable as the reciprocal of flowrate 1/Q. The linear regression models exclude the start delay of the 4th experiment and considers it as an outlier, as shown in Fig. 7(b) with a red triangle. The null hypotheses of these linear regression are that the delays are not a flowrate dependent. These linear regression models are shown in Fig. 7(c). They use six observations implying that they have four degree of freedom. The linear regression model of the start delays shows that the best linear fit of the data is given by values of $\hat{a_0}$ and $\hat{a_1}$ equal to 0.1340 sec and 0.1125 L respectively. The R-squared value of this fit is 0.9414 showing that this model is unable to capture only a mere 6% of the variation. The linear regression model of the end delays shows that the best linear fit of the data is given by values of b_0 and b_1 equal to 0.0161 sec and 0.0745 L respectively. The R-squared value of this fit is 0.8976 indicating that this model cannot explain 10% of the variation. Hence, it is concluded that the delays in start time and end time are flowrate dependent.

The third set of parameters estimated by the particle swarm optimizer was the baseline voltage y_o and voltage rise β for each experiment as shown in Table II. Estimates of the baseline voltage, y_o , show a small degree of drift between experiments. Similar drift is visible when examining the values of the estimated voltage rise, β , for different experiments involving the same CO₂ concentration. For instance, experiments 3, 6, and 7 all pertain to a CO₂ concentration of 16.7%. However, the baseline voltages for these experiments range from 0.121 V to 0.263 V, and the jump in voltage corresponding to a step CO₂ concentration change ranges from 1.85 V to 2.13 V.

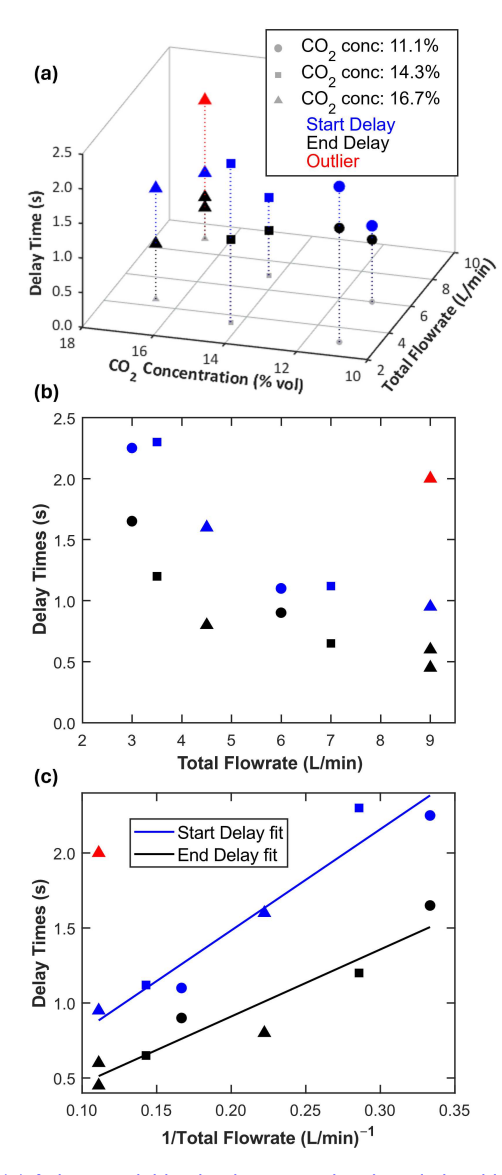


Fig. 7. (a) A three-variable plot demonstrating the relationship between flow rates, CO_2 concentrations, and delay times. (b) Delay times with respective to the flowrates of all seven data points. (c) Impact of fluid flowrate on start/end delays along with their fit curves. There appears to be a linear relationship between delay times and the reciprocal of total flowrate. Note that, in each figure, the outlier is shown in red, whereas the start delay and end delay values are shown in blue and black, respectively. Additionally, the circle, square, and triangle markers represent CO_2 concentrations of 11.1%, 14.3%, and 16.7%, respectively.

Such drift can potentially occur when a nano-photonic sensor is employed in intensity-based demodulation mode, and serves as a strong motivator for wavelength-based demodulation as an alternative. Nevertherless, the value of the experimental characterization work in this paper stems predominantly from the degree to which it furnishes an estimate of the sensor time constant, τ . Such an estimate is potentially useful for understanding the performance limits of the sensor regardless of whether it is used in intensity- or wavelength-based demodulation mode. This creates a strong motivation for characterizing the accuracy of the estimated sensor time constant, as discussed in the next section of this paper.

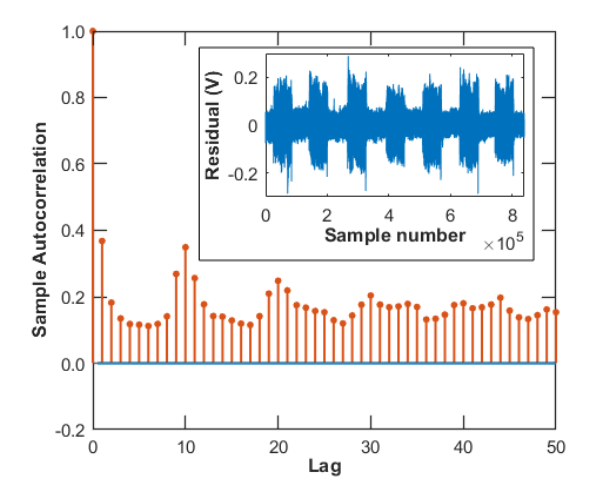


Fig. 8. Auto-correlation plot of the voltage prediction residuals (i.e., differences between measured and predicted voltages). Note that the presence of large auto-correlation values for nonzero lags indicates that the residuals are colored, as opposed to white. Possible explanations include coloring of the raw voltage measurements due to the filtering capabilities of the setup's data acquisition hardware. Figure inset shows the voltage prediction errors/residuals for all 7 experiments, each with 120,000 data points, combined into a single data series.

C. Uncertainty Quantification

To quantify the uncertainties in the above parameter estimates, we begin by analyzing the residuals (i.e., voltage prediction errors) for the above system identification study. The inset within Fig. 8 shows these residuals for all 7 experiments as a single sequence of data points. One observation is that the voltage prediction errors depend on the underlying signal, with higher CO₂ concentrations leading to higher residuals. This is an interesting observation that could potentially be caused by the sensor's underlying characteristics, with larger CO₂ concentrations generating both a larger voltage signal and higher voltage noise. Fig. 8 shows the sample auto-correlation of these voltage residuals. This auto-correlation is colored as opposed to white. This could potentially be caused by signal conditioning circuits/filters within the experimental setup's electronics. While both of these observations are interesting, the magnitudes of the voltage residuals are reasonably small. As a result, the uncertainty quantification study below furnishes reasonable parameter estimation error bounds.

To perform uncertainty quantification, we note that the previous section's system identification problem statement implicitly assumes that the discrepancy between the experimental and identified sensor voltage is solely due to the measurement noise. Then, for any discrete measurement $i=1,\ldots,n$ collected at each time step δt :

$$y_i = \hat{y}_i(\theta) + v_i \tag{13}$$

where y_i is the measured sensor voltage, and $\hat{y}_i(\theta)$ is the identified sensor voltage that depends on the estimated parameter vector $\theta = [\tau, \tau_v, V, (y_0)_1, \ldots, (y_0)_7, \beta_1, \ldots, \beta_7, (t_0)_1, \ldots, (t_0)_7, (t_f)_1, \ldots, (t_f)_7]$. This vector includes the 31 estimated parameters of the model, and v_i is the measurement noise. For simplicity, this measurement noise is assumed to be Gaussian, independent, and identically distributed (iid) with zero mean

and variance σ^2 , $v \stackrel{iid}{\sim} \mathcal{N}(0, \sigma^2)$. This assumption is an approximation of the characteristics of the residuals in Fig. 6, Fig. 8, and the inset within Fig. 8. This approximation simplifies the uncertainty quantification process, with the caveat that the resulting parameter estimation error estimates are themselves approximate. Given these assumptions, the probability density function of the measured sensor voltage is expressed as:

$$f_{\theta}\left(y^{n}\right) = \frac{1}{\left(\sqrt{2\pi\sigma^{2}}\right)^{n}} \exp\left(-\frac{1}{2\sigma^{2}} \sum_{i=1}^{n} \left(y_{i} - \hat{y}_{i}\left(\theta\right)\right)^{2}\right)$$
(14)

Following these assumptions, θ is calculated using the maximum likelihood estimator (MLE) that is given as:

$$\hat{\theta}_{MLE} = \arg\left\{\max f_{\theta}\left(y\right)\right\},\tag{15}$$

which is implemented in Matlab using the particle swarm optimization algorithm, thereby furnishing the least squared error. Generally, the Cramér-Rao Lower Bound (CRLB) can be used for uncertainty quantification assuming that the maximum likelihood estimate of the unknown parameters is asymptotically unbiased. The CRLB theorem states the lowest possible estimate of the covariance of an unbiased estimator equals the inverse of the Fisher information matrix I. For the zero-mean iid Gaussian noise I is given in terms of the sensitivity matrix as follows:

$$I = \frac{1}{\sigma^2} S^T S \tag{16}$$

The sensitivity matrix is constructed by perturbing each element k of θ with an infinitesimal change $\delta\theta_k$ and computing the difference between the perturbed model prediction and true model prediction with respect to the perturbed element of θ_k as follows:

$$S = \begin{bmatrix} s_{1}(\delta t) & s_{2}(\delta t) & \cdots & s_{31}(\delta t) \\ s_{1}(2\delta t) & s_{2}(2\delta t) & \cdots & s_{31}(2\delta t) \\ \vdots & \vdots & \vdots & \vdots \\ s_{1}(n\delta t) & s_{2}(n\delta t) & \cdots & s_{31}(n\delta t) \end{bmatrix}.$$
(17)

Each element of the sensitivity matrix is expressed as:

$$s_{k}(i\delta t) = \lim_{\delta\theta_{k}\to 0} \frac{\hat{y}_{i}(\theta + \delta\theta_{k}) - \hat{y}_{i}(\theta)}{\delta\theta_{k}}$$
(18)

The above equations served as a recipe for applying uncertainty quantification to this paper's parameter estimation results. First, the proposed state-space model was simulated for the optimized parameter value to obtain baseline simulation results. Then the simulation was repeated for a perturbation applied to each parameter independently. This furnished the above sensitivity matrix. Finally, the variance of the voltage estimation residuals, together with this sensitivity matrix, was used to compute the Fisher information matrix I. The inverse of this Fisher information matrix provided Cramér-Rao bounds for the estimation errors associated with these parameters. More specifically, each diagonal term in the resulting CRLB matrix provided an estimation variance for the corresponding parameter. Computing the square root of this variance and multiplying by 3 finally furnished the $\pm 3\sigma$ estimation errors

TABLE III
BOUNDS ON THE MODEL PARAMETERS

Parameter	Bound		
Sensor's time constant $ au$	$\pm 5.6049 \text{ (ms)}$		
Setup's actuation time constant $ au_v$	±8.6029 (ms)		
Manifold volume V	±0.6817 (mL)		

for the parameter. Table III lists these estimation errors for the three time constants associated with the sensor, setup actuator, and manifold volume. All of these error bounds are small compared to the nominal parameter estimates. This highlights the degree to which the approach proposed in this paper can enable the characterization of a fast nano-photonic sensor, even when the dynamics of the underlying setup are much slower than the sensor.

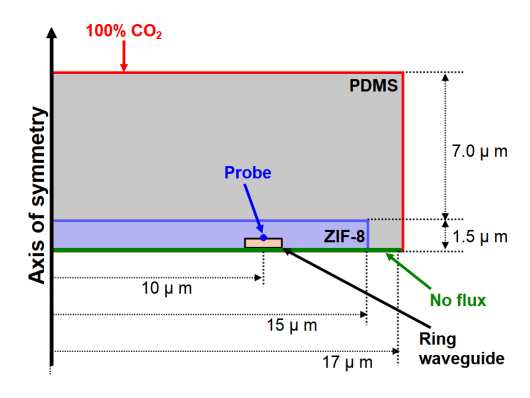
D. Finite Element Analysis of Sensor Time Constant

Finite element analysis was carried out to validate the estimated sensor time constant. COMSOL Multiphysics (using the Transport of Diluted Species interface) was used to model and simulate the gas diffusion across the ZIF-8/PDMS coating layer. Fig. 9(a) shows the 2D model of the ZIF-8/PDMS coating layer of the sensor. The radius of the ring resonator is 10 µm, and the thickness of the ZIF-8 and PDMS coating layers is 1.5 µm and 7.0 µm, respectively. The gas diffusion was simulated based on Fick's law of diffusion as:

$$\frac{\partial c}{\partial t} + \nabla \cdot (-D\nabla c) = 0 \tag{19}$$

where c is the gas concentration, D is the diffusion coefficient, and t is time. The diffusion coefficients of CO_2 gas in the ZIF-8 and PDMS were set to 1.71×10^{-10} m²/s [21] and 4.2×10^{-9} m²/s [22], respectively. The gas concentration on the top and right boundaries was set to 100 CO_2 Vol %, while the bottom boundary was set to a No Flux condition. The initial condition was set to 0 CO_2 Vol %. The point for checking the gas concentration is positioned 220 nm above the bottom boundary and is annotated as Probe. Note that this simulation can be extended for light and heavy gas/vapor other than CO_2 , provided that the diffusion coefficients of the gas/vapor in ZIF-8 and PDMS are available.

The change in gas concentration at Probe is presented as the red curve in Fig. 9(b). The simulated time constant is 12.9 msec, which is smaller than the estimated 48 msec. One of the causes of this discrepancy is believed to be fabrication errors. The ZIF-8 layer in the sensor was coated manually with a dip coating process, which is suspected to have affected the variation of film properties. For example, the refractive index of ZIF-8, one of its material properties, varies across literature from 1.34 to 1.49 refractive index unit (RIU) despite using the same synthesis process [7], [23]. Similar to the refractive index, we believe that such a coating process could affect the diffusion coefficient. In case the diffusion coefficient of ZIF-8 is set to 2.6×10^{-11} m²/s, approximately 15% of the reference value, the simulated time constant becomes comparable to



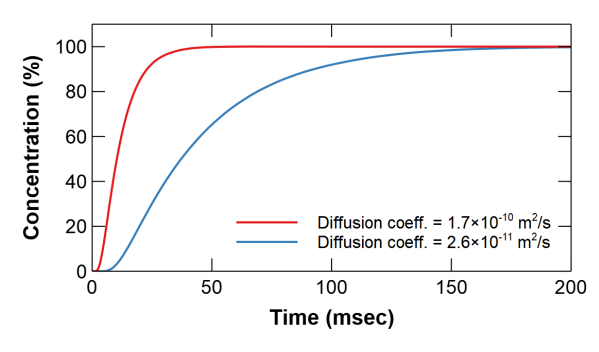


Fig. 9. (a) 2D simulation model for the gas diffusion across the ZIF-8/PDMS coating layer. (b) Time-dependent simulation of the gas concentration at Probe with two different diffusion coefficients of ZIF-8

the estimated value of 48 msec, shown as the blue curve in Fig. 9(b). Therefore, considering these simulation results and fabrication errors, we believe the system identification method estimated the sensor time constant with reasonable accuracy.

IV. DISCUSSION AND CONCLUSIONS

We successfully characterized the dynamic response of a fast-responding nanophotonic dissolved CO₂ sensor using optimization-based system identification. The nanophotonic sensor employed a silicon ring resonator with ZIF-8/PDMS cladding for dissolved CO₂ gas sensing. Seven experimental conditions with different CO2 concentrations and different gas flow rates were used for characterizing the dynamic response of the sensor. After applying Matlab's implementation of particle swarm optimization algorithm on the acquired experimental results, the sensor's time constant was estimated to be 48.1±5.6 ms. Considering the simulated time constant and errors in ZIF-8 fabrication, we believe the system identification method estimated the sensor time constant with reasonable accuracy. The proposed approach will offer a cost-effective method for characterizing various fast responding sensors using conventional test systems with slower responses than the sensor response.

REFERENCES

[1] Y. Ma, B. Dong, and C. Lee, "Progress of infrared guided-wave nanophotonic sensors and devices," *Nano Convergence*, vol. 7, no. 1, pp. 1–34, 2020.

- [2] W. Jin, H. Ho, Y. Cao, J. Ju, and L. Qi, "Gas detection with microand nano-engineered optical fibers," *Optical Fiber Technology*, vol. 19, no. 6, pp. 741–759, 2013.
- [3] H. Yuan, N. Li, W. Fan, H. Cai, and D. Zhao, "Metal-organic framework based gas sensors," *Advanced Science*, vol. 9, no. 6, p. 2104374, 2022.
- [4] R. J. Kuppler, D. J. Timmons, Q.-R. Fang, J.-R. Li, T. A. Makal, M. D. Young, D. Yuan, D. Zhao, W. Zhuang, and H.-C. Zhou, "Potential applications of metal-organic frameworks," *Coordination Chemistry Reviews*, vol. 253, no. 23-24, pp. 3042–3066, 2009.
- [5] H. Furukawa, K. E. Cordova, M. O'Keeffe, and O. M. Yaghi, "The chemistry and applications of metal-organic frameworks," *Science*, vol. 341, no. 6149, p. 1230444, 2013.
- [6] G. Lu and J. T. Hupp, "Metal- organic frameworks as sensors: a ZIF-8 based fabry- pérot device as a selective sensor for chemical vapors and gases," *Journal of the American Chemical Society*, vol. 132, no. 23, pp. 7832–7833, 2010.
- [7] H.-T. Kim, W. Hwang, Y. Liu, and M. Yu, "Ultracompact gas sensor with metal-organic-framework-based differential fiber-optic fabry-perot nanocavities," *Optics Express*, vol. 28, no. 20, pp. 29 937–29 947, 2020.
- [8] J. Tao, X. Wang, T. Sun, H. Cai, Y. Wang, T. Lin, D. Fu, L. L. Y. Ting, Y. Gu, and D. Zhao, "Hybrid photonic cavity with metal-organic framework coatings for the ultra-sensitive detection of volatile organic compounds with high immunity to humidity," *Scientific reports*, vol. 7, no. 1, pp. 1–8, 2017.
- [9] K.-J. Kim, P. Lu, J. T. Culp, and P. R. Ohodnicki, "Metal-organic framework thin film coated optical fiber sensors: a novel waveguidebased chemical sensing platform," ACS sensors, vol. 3, no. 2, pp. 386– 394, 2018.
- [10] L. E. Kreno, J. T. Hupp, and R. P. Van Duyne, "Metal- organic framework thin film for enhanced localized surface plasmon resonance gas sensing," *Analytical chemistry*, vol. 82, no. 19, pp. 8042–8046, 2010.
- [11] X. Chong, K.-J. Kim, P. R. Ohodnicki, E. Li, C.-H. Chang, and A. X. Wang, "Ultrashort near-infrared fiber-optic sensors for carbon dioxide detection," *IEEE Sensors Journal*, vol. 15, no. 9, pp. 5327–5332, 2015.
- [12] K.-J. Kim, X. Chong, P. B. Kreider, G. Ma, P. R. Ohodnicki, J. P. Baltrus, A. X. Wang, and C.-H. Chang, "Plasmonics-enhanced metalorganic framework nanoporous films for highly sensitive near-infrared absorption," *Journal of Materials Chemistry C*, vol. 3, no. 12, pp. 2763–2767, 2015.
- [13] X. Chong, K.-J. Kim, E. Li, Y. Zhang, P. R. Ohodnicki, C.-H. Chang, and A. X. Wang, "Near-infrared absorption gas sensing with metal-organic framework on optical fibers," *Sensors and Actuators B: Chemical*, vol. 232, pp. 43–51, 2016.
- [14] H. Zhou, X. Hui, D. Li, D. Hu, X. Chen, X. He, L. Gao, H. Huang, C. Lee, and X. Mu, "Metal-organic framework-surface-enhanced infrared absorption platform enables simultaneous on-chip sensing of greenhouse gases," *Advanced Science*, vol. 7, no. 20, p. 2001173, 2020.
- [15] J. P. Norton, An introduction to identification. Courier Corporation, 2009.
- [16] L. Ljung, System identification. Springer, 1998.
- [17] J. Fraden and J. Fraden, Handbook of modern sensors: physics, designs, and applications. Springer, 2010, vol. 3.
- [18] W. Bogaerts, P. De Heyn, T. Van Vaerenbergh, K. De Vos, S. Kumar Selvaraja, T. Claes, P. Dumon, P. Bienstman, D. Van Thourhout, and R. Baets, "Silicon microring resonators," *Laser & Photonics Reviews*, vol. 6, no. 1, pp. 47–73, 2012.
- [19] I. M. White and X. Fan, "On the performance quantification of resonant refractive index sensors," *Optics express*, vol. 16, no. 2, pp. 1020–1028, 2008.
- [20] H.-T. Kim, B. Ramdam, and M. Yu, "Silicon ring resonator with ZIF-8/PDMS cladding for sensing dissolved CO2 gas in perfluorocarbon solutions," Sensors and Actuators B: Chemical, p. 135305, 2024.
- [21] B. Bayati, A. Ghorbani, K. Ghasemzadeh, A. Iulianelli, and A. Basile, "Study on the separation of h2 from co2 using a ZIF-8 membrane by molecular simulation and maxwell-stefan model," *Molecules*, vol. 24, no. 23, p. 4350, 2019.
- [22] A.-J. Mäki, M. Peltokangas, J. Kreutzer, S. Auvinen, and P. Kallio, "Modeling carbon dioxide transport in pdms-based microfluidic cell culture devices," *Chemical Engineering Science*, vol. 137, pp. 515–524, 2015.
- [23] J. Hromadka, B. Tokay, S. James, R. P. Tatam, and S. Korposh, "Optical fibre long period grating gas sensor modified with metal organic framework thin films," *Sensors and Actuators B: Chemical*, vol. 221, pp. 891–899, 2015.